Targeted search for the stochastic gravitational-wave background from the galactic millisecond pulsar population

Deepali Agarwal,[1,*] Jishnu Suresh,[2,†] Vuk Mandic,[3,‡] Andrew Matas,[4,§] and Tania Regimbau[5,‖]

[1]*Inter-University Centre for Astronomy and Astrophysics (IUCAA), Pune 411007, India*
[2]*Centre for Cosmology, Particle Physics and Phenomenology (CP3), Université catholique de Louvain, B-1348 Louvain-la-Neuve, Belgium*
[3]*University of Minnesota, Minneapolis, Minnesota 55455, USA*
[4]*Max Planck Institute for Gravitational Physics (Albert Einstein Institute), D-14476 Potsdam, Germany*
[5]*Laboratoire d'Annecy de Physique des Particules, CNRS, 9 Chemin de Bellevue, 74941 Annecy, France*

(Received 28 April 2022; accepted 19 July 2022; published 19 August 2022)

The millisecond pulsars, old-recycled objects spinning with high frequency $\mathcal{O}$ (kHz) sustaining the deformation from their spherical shape, may emit gravitational waves (GW). These are one of the potential candidates contributing to the anisotropic stochastic gravitational-wave background (SGWB) observable in the ground-based GW detectors. Here, we present the results from a likelihood-based targeted search for the SGWB due to millisecond pulsars in the Milky Way, by analyzing the data from the first three observing runs of Advanced LIGO and Advanced Virgo detector. We assume that the shape of SGWB power spectra and the sky distribution is known *a priori* from the population synthesis model. The information of the ensemble source properties, i.e., the in-band number of pulsars, $N_{\rm obs}$ and the averaged ellipticity, μ_ϵ is encoded in the maximum likelihood statistic. We do not find significant evidence for the SGWB signal from the considered source population. The best Bayesian upper limit with 95% confidence for the parameters are $N_{\rm obs} \leq 8.8 \times 10^4$ and $\mu_\epsilon \leq 1.4 \times 10^{-6}$, which is comparable to the bounds on mean ellipticity with the GW observations of the individual pulsars. Finally, we show that for the plausible case of $N_{\rm obs} = 40000$, with the one year of observations, the one-sigma sensitivity on μ_ϵ might reach 1.5×10^{-7} and 4.1×10^{-8} for the second-generation detector network having A+ sensitivity and third-generation detector network, respectively.

DOI: 10.1103/PhysRevD.106.043019

I. INTRODUCTION

Dozens of gravitational-waves (GWs) sources have been cataloged [1–3] using the data from the recently completed third observing run (O3) of Advanced LIGO [4] and Advanced Virgo [5] detectors. These sources fall under the compact binary coalescence (CBC) category, particularly binary-black-hole mergers, binary-neutron-star mergers, and black-hole-neutron star mergers, whose signal lasts for seconds. The continuous GWs and stochastic gravitational-wave background (SGWB) are the interesting source categories yet to be detected. The continuous GWs is a persistent form of the gravitational radiation emitted at a nearly fixed frequency from a quadruple variation of matter, e.g., spinning neutron stars in isolated/binary system [6]. On the other hand, the SGWB is also a persistent signal but resultant of the incoherent superposition of GWs from a large number of sources with cosmological (e.g., inflationary GWs) and astrophysical origin (e.g., CBCs and neutron stars, etc.), and hence random in nature [7]. It is expected that the weak GW sources that are individually undetectable will produce a SGWB whose collective, incoherent signal will be detectable.

The SGWB can be categorized based on different angular distributions, i.e., isotropic and anisotropic or/and spectral distribution properties, i.e., broadband (with a power-law spectral model specific to source population) and narrow band sources. The astrophysical sources are also expected to produce anisotropic signal [8–20], and the upper limits placed on the estimator of SGWB amplitude [8,21,22] by isotropic searches could lead to conservative limits. The isotropic and directional searches were performed for the broadband SGWB combining the estimators from multiple frequency bins weighted by a power-law spectral model using the data from several runs of Advanced LIGO and Advanced Virgo detectors [23,24].

In the past, a likelihood-based formalism was proposed and discussed in Refs. [21,25,26], to perform a targeted search for an extended anisotropic SGWB knowing *a priori*, its angular distribution along with the spectral properties.

*deepali@iucaa.in
†jishnu.suresh@uclouvain.be
‡vuk@umn.edu
§andrew.matas@aei.mpg.de
‖regimbau@lapp.in2p3.fr

This can improve the sensitivity of the search for the extended sources considerably. In this work, we adopt a similar formalism and perform a targeted search for the SGWB formed by the Galactic millisecond pulsars population, using the data from the first three observing runs (O1, O2, and O3) of Advanced LIGO and Advanced Virgo observatories.

Out of 10^8–10^9 neutron stars in the Milky Way galaxy [27], ∼40000 recycled and rotation powered pulsars are expected to spin with period < 30 ms [28] called millisecond pulsars (MSPs). The MSPs with the asymmetric deformations around its spin axis (spinning with frequency f) may emit "monochromatic" continuous GWs (at frequency $2f$) in the frequency range of several 100 Hz to about 1 kHz where the ground-based GW detectors are sensitive.[1] For a nonprecessing triaxial body with the spin axis along the z axis, the GW strain amplitude is proportional to the deformation parameter called ellipticity ϵ and is defined as

$$\epsilon = \frac{I_{xx} - I_{yy}}{I_{zz}}, \tag{1}$$

where I_{xx}, I_{yy}, and I_{zz} are the principal moments of inertia (or xx, yy, and zz component). In practice, the ellipticity is very small, i.e., $|\epsilon| \ll 1$ and $I_{xx} \simeq I_{yy} \simeq I_{zz} = I$.

The neutron stars can serve as an astrophysical laboratory to probe the equation of states of matter at several nuclear saturation densities. The maximum deformation of the neutron star is a function of the equation of state, i.e., a stiffer equation of state allows larger deformations than the softer ones. Thus measuring the ellipticity can constrain the equation of state. The maximum ellipticity due to thermal pressure perturbation lies in the range 10^{-10}–10^{-7} for different chiral effective-field-theory equation-of-state models [30]. Cutler [31] claimed the ellipticity in range $\epsilon \sim 10^{-9}$–10^{-8} caused by the internal toroidal magnetic field for millisecond pulsars. Also, since the spin-down observed in the electromagnetic observations is due to GW emission, an average upper limit ellipticity of $\sim 10^{-8}$ is calculated for millisecond pulsars called spin-down limit. The targeted search for GW signals from a nearby recycled pulsar (PSR J0711 − 6830) has bound ellipticity to be $\epsilon \leq 5.3 \times 10^{-9}$, which surpasses the indirect spin-down limit [32]. We note that there is evidence for the existence of minimum ellipticity $\epsilon \geq 10^{-9}$, which indicates that GW radiation might be the dominant mechanism for the spin-down of MSPs [33].

Due to the weak signal strength, the individual detection of GWs produced by MSPs at a far distance (Galactic and extragalactic) may not be possible. However, these are potential candidates which contribute to the astrophysical SGWB [21,22,26,34,35]. Hence, the SGWB searches can detect GWs from ensemble of MSPs and can give us more information about the MSPs' ensemble properties, like the number of MSPs within the search band (in-band number) and the average ellipticity.

The paper is structured as follows. In Sec. II, we review the formalism for performing a cross-correlation-based targeted search for an anisotropic SGWB and derive a maximum likelihood statistic for the "overall amplitude" of the SGWB. In Sec. III, we discuss the MSP population synthesis model, which we adopt to perform the stochastic search. We will also illustrate the method to prepare a template for the spatial distribution. Details about the data and analysis pipeline are given in Sec. IV. Following the analysis outlined in the previous section, we present the results from the search in Sec. V. In Sec. VI, we will show the forecast on the expected sensitivity with the future detector network. We will conclude the article with the future prospects of the search in Sec. VII.

II. SGWB SEARCH METHODS

Considering the GW strain data from two geographically separated detectors, the SGWB signal is expected to be correlated while the detector noise is uncorrelated. Hence, the searches [23,24] for SGWB are performed by constructing a cross-correlation spectral density (CSD) for a given baseline $\mathcal{I}$ (formed with the two detectors 1 and 2) as

$$C_{\mathcal{I}}(t;f) = \frac{2}{\tau}\tilde{s}_1^*(t;f)\tilde{s}_2(t;f), \tag{2}$$

where $\tilde{s}_1$ and $\tilde{s}_2$ are the short-term Fourier transforms of the strain time series data of segment duration τ from detector 1 and 2 and centered around the time labeled by t. The expected value of $C_{\mathcal{I}}(t;f)$ is related to the one-sided power spectral density (PSD) $\mathcal{P}_{\hat{\Omega}}(f)$ of the incoming GWs in the frequency range f and $f + \mathrm{d}f$ per solid angle $\mathrm{d}^2\hat{\Omega}$, if the source is in the direction $\hat{\Omega}$, as

$$\langle C_{\mathcal{I}}(t;f)\rangle = \int \mathrm{d}^2\hat{\Omega}\gamma^{\mathcal{I}}_{\hat{\Omega}}(t;f)\mathcal{P}_{\hat{\Omega}}(f). \tag{3}$$

Here, $\gamma^{\mathcal{I}}_{\hat{\Omega}}$ denotes a detector-geometry dependent function, usually referred to as the overlap reduction function (ORF). The information of the detector response is encoded in this ORF, and it varies with the sidereal time, location of the detectors, and the frequency of the signal [7,25,36,37]. We note that the observed CSD represents the signal from the collection of sources convolved with the detector response.

The source strain PSD $\mathcal{P}_{\hat{\Omega}}(f)$ can be decomposed into the orthogonal bases $e_\alpha(\hat{\Omega})$, suitable to the angular distribution of the sources in the sky as

$$\mathcal{P}_{\hat{\Omega}}(f) = e_\alpha(\hat{\Omega})\mathcal{P}_\alpha(f), \tag{4}$$

using the Einstein sum convention. Depending on the source angular distribution, one can choose the basis

[1]Several other mechanisms of the spinning neutron stars will also produce GWs, e.g., r modes [29].

function $e_\alpha(\hat{\Omega})$. The pixel basis $e_\alpha(\hat{\Omega}) = \delta^2(\hat{\Omega} - \hat{\Omega}_\alpha)$ is the preferred choice for a point source where as the spherical harmonic basis $e_\alpha(\hat{\Omega}) = Y_{l,m}(\hat{\Omega})$ is usually used for the extended source distributions. The unit of the elements $\mathcal{P}_\alpha(f)$ is $\mathrm{Hz}^{-1}\,\mathrm{sr}^{-\frac{1}{2}}$ in the spherical harmonic basis while Hz^{-1} in the pixel basis. The analysis reported in this paper make use of the pixel basis to report the results. So, using Eq. (3) one can write the expected value of the CSD and the ORF, respectively, as

$$\langle C_{\mathcal{I}}(t;f)\rangle = \gamma^{\mathcal{I}}_\alpha(t;f)\mathcal{P}_\alpha(f), \tag{5}$$

$$\gamma^I_\alpha(t;f) = \int \mathrm{d}^2\hat{\Omega}\gamma^{\mathcal{I}}_{\hat{\Omega}}(t;f)e_\alpha(\hat{\Omega}). \tag{6}$$

In practice, we combine estimators from multiple time segments (∼80000), multiple baselines, and the frequency bins (when searching for broadband signal) to obtain a broadband "average" estimator of source strain PSD. In such cases, from both a central limit theorem and a weak signal limit, the CSD is expected to follow a Gaussian distribution with variance $P_1(t;f)P_2(t;f)$ [38]. Here $P(t,f)$ is the one-sided noise PSD for the individual detector. Now one can write the combined likelihood L for the CSD as

$$L \propto \prod_{\mathcal{I}t,f} \exp\Bigg[-\frac{1}{2}(C_{\mathcal{I}}(t;f) - \gamma^{\mathcal{I}}_\alpha(t;f)\mathcal{P}_\alpha(f))^* \times \frac{1}{P_1(t;f)P_2(t;f)}(C_{\mathcal{I}}(t;f) - \gamma^{\mathcal{I}}_{\alpha'}(t;f)\mathcal{P}_{\alpha'}(f))\Bigg]. \tag{7}$$

If, we further decompose the source strain PSD in terms of a frequency dependent factor $\bar{H}_f$, a direction dependent factor $\hat{\mathcal{P}}_\alpha$ and an "overall amplitude" denoted by a scalar A, then

$$\mathcal{P}_\alpha(f) = A\bar{H}_f\hat{\mathcal{P}}_\alpha. \tag{8}$$

Detailed discussions on the astrophysical origin of the quantities in the right hand side of the above equation are given in Sec. III. Assuming that the $\bar{H}_f$ and $\hat{\mathcal{P}}_\alpha$ are confidently known, then maximum likelihood (ML) estimator of A and its mean $\langle A\rangle$ are given as [25,26]

$$\hat{A} = \frac{\mathbf{X}^\dagger\hat{\boldsymbol{\mathcal{P}}}}{\hat{\boldsymbol{\mathcal{P}}}^\dagger\boldsymbol{\Gamma}\hat{\boldsymbol{\mathcal{P}}}}, \qquad \langle\hat{A}\rangle = A. \tag{9}$$

Here $\mathbf{X}$ is the "dirty map,"

$$\mathbf{X} \equiv X_\alpha = \sum_{\mathcal{I}t,f}\frac{C_{\mathcal{I}}(t;f)\gamma^{\mathcal{I}*}_\alpha(t;f)\bar{H}_f}{P_1(t;f)P_2(t;f)}, \tag{10}$$

and $\boldsymbol{\Gamma}$ represents the Fisher information matrix [25,37],

$$\boldsymbol{\Gamma} \equiv \Gamma_{\alpha,\alpha'} = \sum_{\mathcal{I}t,f}\frac{\gamma^{\mathcal{I}*}_\alpha(t;f)\gamma^{\mathcal{I}}_{\alpha'}(t;f)\bar{H}^2_f}{P_1(t;f)P_2(t;f)}. \tag{11}$$

Following these definitions, it is straightforward to write the likelihood in Eq. (7) in terms of the dirty map and Fisher information matrix as

$$L \propto \exp\left[-\frac{1}{2}(\mathbf{X} - A\boldsymbol{\Gamma}.\hat{\boldsymbol{\mathcal{P}}})^\dagger\boldsymbol{\Gamma}^{-1}(\mathbf{X} - A\boldsymbol{\Gamma}.\hat{\boldsymbol{\mathcal{P}}})\right]. \tag{12}$$

It is interesting to note that the ML estimator, $\hat{A}$ has a similar form to the matched-filter statistic used in CBC searches [39]. In our analysis, we are essentially "matching" the observed dirty map with the model describing the sky distribution of the source power. The model is obtained by convolving the template $\hat{\boldsymbol{\mathcal{P}}}$, sky distribution known *a priori*, with the detector response (i.e., the forward modeling). From the likelihood, the variance and signal-to-noise ratio (SNR) of $\hat{A}$ are given as [25,26]

$$\sigma^2_{\hat{A}} = \frac{1}{\hat{\boldsymbol{\mathcal{P}}}^\dagger\boldsymbol{\Gamma}\hat{\boldsymbol{\mathcal{P}}}}, \tag{13}$$

$$\rho_{\hat{A}} = \frac{\mathbf{X}^\dagger\hat{\boldsymbol{\mathcal{P}}}}{\sqrt{\hat{\boldsymbol{\mathcal{P}}}^\dagger\boldsymbol{\Gamma}\hat{\boldsymbol{\mathcal{P}}}}}. \tag{14}$$

The Gaussian nature of the CSD makes sure that the dirty map $\mathbf{X}$, the ML estimator $\hat{A}$ of the amplitude A, and its SNR $\rho_{\hat{A}}$ follow the Gaussian distribution with their mean and variance. These properties will be useful in assigning the significance to the observed data and setting the upper limit on the source parameters in case of no detection.

It is also interesting that if the template is a vector with a single nonzero element, having a value equal to 1, then $\hat{A}$ is equivalent to the broadband radiometer search estimator, a measure of the strength of the GWs signal from a pixel or (l,m) mode in the sky [24]. On the other hand, if the template is a vector with the elements having a value of 1, then $\hat{A}$ is identical to the isotropic search estimator [23].

In the usual map-making process, a "clean map" is the ML estimator of the "true" sky map $\hat{\boldsymbol{\mathcal{P}}}$ obtained through deconvolution process [25,37,40,41]. It is also possible to rewrite the likelihood given in Eq. (12) to obtain the ML estimator $\hat{A}$ of the amplitude in terms of this clean map [26]. However, the deconvolution involves the inversion of the highly ill-conditioned Fisher information matrix. Due to the insensitivity of the detector to certain modes/directions in the sky, the inversion of the Fisher matrix leads to the inverted noise boost [25,37,41–43], thus making the deconvolution process a challenge. We choose to work with the dirty map and avoid unnecessary information loss and numerical errors that may arise in the regularization process.

III. MSP POPULATION SYNTHESIS MODEL

In this section, we will be discussing the expected PSD of the MSP population. The strain PSD for SGWB signal from the neutron star population emitting GWs in the frequency range f to $f + \mathrm{d}f$ and lying in solid angle $\hat{\Omega}$ and $\hat{\Omega} + \mathrm{d}^2\hat{\Omega}$ is given by (see the Appendix)

$$\mathcal{P}(f,\hat{\Omega}) = \underbrace{N_{\rm obs}\langle\epsilon^2\rangle_s}_{A}\underbrace{f^4 p(f)}_{H_f}\frac{32\pi^4 G^2\langle I^2\rangle_s}{5c^8}\langle r^{-2}\rangle_s p(\hat{\Omega}). \tag{15}$$

Since we are working in the pixel basis, the elements of the template $\hat{P}$ are given by

$$\hat{P}_\alpha = \int_{\hat{\Omega}_\alpha}^{\hat{\Omega}_\alpha + d\hat{\Omega}_\alpha}\frac{32\pi^4 G^2\langle I^2\rangle_s}{5c^8}\langle r^{-2}\rangle_s p(\hat{\Omega})d\hat{\Omega} \tag{16}$$

Above $N_{\rm obs}$ is the total number of neutron stars within the observing band and sky patch. Therefore,

$$N_{\rm obs} = \int_{f_{\rm min}}^{f_{\rm max}}\mathrm{d}f\, p(f)\int_{\rm sky}\mathrm{d}\hat{\Omega}\pi_{\hat{\Omega}}\int_0^\infty \mathrm{d}r\, r^{-2}p(r), \tag{17}$$

where $f_{\rm min}$ and $f_{\rm max}$ are, respectively, the lower and upper limits of the observed frequency band. The probability density of a MSP to be observed in the direction $\hat{\Omega}$ at distance r from the Earth and emitting GWs at frequency f are encoded in $p(\hat{\Omega})$, $p(r)$, and $p(f)$. The parameters I and ϵ are the principle moment of inertia and deformation parameter called ellipticity [Eq. (1)] of each neutron star. The $\langle\ldots\rangle_s$ denotes the ensemble average over the source population. The subscript "s" in the angular bracket is introduced to distinguish it from the ensemble average over noise in Eq. (9). In this study, we will be using a fiducial value of $\langle I^2\rangle_s = (1.1\times 10^{38}\ \mathrm{kgm}^2)^2$, which is constrained very well from nuclear physics studies [44].

In order to describe the SGWB signal from the Galactic MSPs, a model of their spatial and frequency distribution is required. The determination of the intrinsic distribution of the spin-period, magnetic field, period derivative, and spatial coordinates for the MSPs is an ambitious goal in the field of electromagnetic astronomy as well. There have been studies to understand the underlying distribution based on the statistical analyses of artificial MSPs that pass the criteria for detection and comparing them with the detected MSPs [28,45–47]. Next, we will discuss the model adopted for the spectral shape and the template for the spatial distribution constrained by electromagnetic observations.

A. Frequency dependence model

The likelihood analysis of a sample of ∼56 radio MSPs observed in the "first generation" of Parkes multibeam surveys [48–53] found that the underlying distribution of the spin period of MSPs can be best fitted with log-normal function form. Interestingly, these findings are consistent with the current (large) sample of ∼206 MSPs within a 95% credible region [46]. For our analysis, we consider the best fit parameter values, as given in Lorimer *et al.* [46]. We also modify the probability density function (PDF) by changing the spin-period P to the GW frequency variable $f = 2/P$ (Hz) to well suit the analysis described in this paper. The modified PDF is given as

$$p(f|\mu,\sigma) = \frac{1}{\sqrt{2\pi}f\sigma}\exp\left[-\frac{(\ln(f)-\mu)^2}{2\sigma^2}\right], \tag{18}$$

with mean $\mu = 6.1$ and variance $\sigma = 0.58$. The probability density profile for the GW frequency and the spectral shape of SGWB using Eq. (15) are illustrated in Figs. 1(a) and 1(b), respectively. Note that the peak of PDF at ∼400 Hz is disappeared in the figure showing the spectral shape of SGWB, since the luminosity of individual MSP scales as f^6 [see Eq. (A3)].

B. Spatial distribution model

One can write the radial and height distribution for the MSP population in terms of the exponential functions as

$$p(R,z) \propto \exp(-R/R_0)\exp(-|z|/z_0), \tag{19}$$

where R and z (having unit kpc in the galactocentric coordinate system) define the pulsar's distance from the Galactic Center and the height of the pulsar above the Galactic plane. We use the best-fit values for the parameters $R_0 \approx 4$ kpc and $z_0 \approx 1$ kpc as given in Grégoire, T. and Knödlseder, J. [47]. The polar axis passes through the Galactic Center perpendicular to the Galactic plane. The PDF for polar angle ϕ can be assumed to be uniform between $[0, 2\pi]$ with $\phi = 0$ measured along the axis connecting the Galactic Center to Earth. On the other hand, other models for the radial distribution of MSPs are also explored in the literature [28] by considering a half-Gaussian distribution function as

$$p(R,z) \propto \exp(-R^2/2\Sigma_r^2)\exp(-|z|/z_0), \tag{20}$$

where the radial and vertical heights are constrained to be $\Sigma_r = 7.5$ kpc and $z_0 \approx 0.5$ kpc from the statistical analysis of the observed MSPs in radio band along with the uniform distribution for the polar angle. In this work, we will analyze the data considering both the PDFs for radial coordinate. The template or model map $\hat{\mathcal{P}}$ is obtained by following the steps given below:

(1) We draw random locations of $N = 10^5$ pulsars with the density function given above in terms of galactocentric coordinates $\{R, z, \phi\}$.

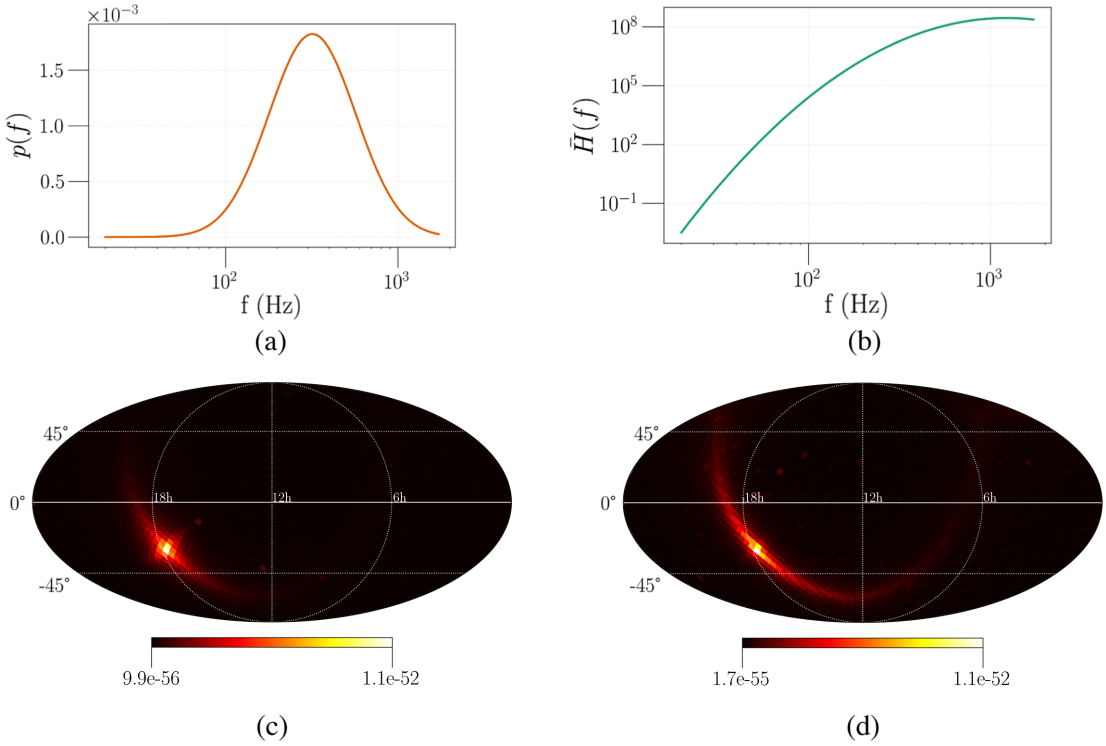

FIG. 1. The MSP population synthesis model used in the analysis. (a) The probability density profile, $p(f)(f)$ as a function of the GW frequency f. (b) The expected spectral dependence $\bar{H}(f)$ of SGWB signal. The maps (c) and (d) represent the template $\hat{\mathcal{P}}$ for the spatial distribution of the source power with exponential and Gaussian density profiles for the radii, respectively.

(2) We then convert the pulsar positions from galactocentric coordinates $\{R, z, \phi\}$ to equatorial coordinates $\{\mathrm{RA}, \mathrm{Dec}, r\}$. Here, we assumed the sun to be at 8.12 kpc away from the Galactic Center [54] and at 20.8 pc height [55] above the Galactic plane.
(3) Next the simulated pulsar are binned into 3072 HEALPix pixels with $\mathrm{n_{side}} = 16$ [56,57]. We then calculate r^{-2} for each pulsar and compute the average over that for each pixels [see Eq. (A2) for a detailed derivation].

The final step described above gives us the map of $\langle r^{-2}\rangle p(\hat{\Omega})$. We multiply it with the constant [see Eq. (16)] to obtain $\hat{\mathcal{P}}$. We then create 1000 such realizations following the above three steps recursively. The average of these realizations is considered as the template for the MSP population. It is worth mentioning that, by considering the mean of these realizations, one can suppress the large power (statistical fluctuations) from the pulsars outside of the Galactic plane. The templates for both the exponential distribution and the Gaussian distribution of the radial coordinate are shown in Figs. 1(c) and 1(d), respectively.

Given these population properties, we are interested in constraining the ensemble properties of MSPs, i.e., N_{obs} and averaged ellipticity μ_ϵ. However, the estimator A of our search has information on the average of squared ellipticity, $\langle\epsilon^2\rangle_s$ [Eq. (15)], which is related to the μ_ϵ as

$$\langle\epsilon^2\rangle_s = \mu_\epsilon^2 + \Sigma_\epsilon^2. \tag{21}$$

Estimating intrinsic variance Σ_ϵ of ellipticity requires its distribution to be known. However, the actual distribution is not confidently known. Thus, we assume

$$\langle\epsilon^2\rangle_s = \mu_\epsilon^2 \Rightarrow A = N_{\mathrm{obs}}\mu_\epsilon^2. \tag{22}$$

The above approximation is valid if the intrinsic variance is small compared to the averaged ellipticity, i.e., $\Sigma_\epsilon \ll \mu_\epsilon$. Even though this leads to bias in the estimator, in the rest of the paper, we assume this approximation is valid [21,22].

IV. DATA AND PIPELINE

For the analysis, we use the data from the first three observing runs (O1, O2, and O3) of Advanced LIGO's Hanford (H) and Livingston (L) and Advanced Virgo (V) detectors calibrated by LIGO-Virgo-KAGRA collaboration [58–60]. The data is now available publicly [61,62]. The strain time-series data is processed in a similar way as in Abbott *et al.* [24,63,64] to obtain the CSDs for individual datasets/baselines, i.e., O1-HL, O2-HL, and HL, LV, and HV in O3 run, as well as the PSDs for individual detectors. These quantities are computed for the segments of $\tau = 192$ s long duration and $1/32$ Hz frequency resolution along with the observing band of 20–1726 Hz [see Eq. (2)]. The data

quality cuts in the time domain and the frequency domain to remove the non-Gaussian features and the known artifacts are applied identically as in Abbott *et al.* [24,63,64]. The CSDs and PSDs are further compressed to one sidereal day using the folding algorithm [38,65]. In the next step, we prepare the dirty map $\mathbf{X}$ [Eq. (10)] and the Fisher information matrix $\mathbf{\Gamma}$ [Eq. (11)] for each baseline with the folded data and PyStoch pipeline [66] in HEALPix grid of 3072 pixels in pixel basis. The dirty map and the Fisher information matrix for the combined network (O1+O2+O3) can be obtained by combining the estimators from individual baselines/observing runs using Eqs. (10) and (11).

V. OBSERVATIONAL RESULTS

With the observed data, we estimate the overall amplitude $\hat{A}$ [Eq. (9)] and its SNR $\rho_{\hat{A}}$ [Eqs. (13) and (14)], using the prepared dirty map and Fisher matrix for individual datasets and combined network ($\mathrm{O1}+\mathrm{O2}+\mathrm{O3}$) along with the prepared templates $\hat{\mathcal{P}}$ as detailed in Sec. III B. The results of the analysis are obtained in two steps. First, the observed data is assessed against the null hypothesis by assigning the p values. In the second step, we determine the 90% confidence credible intervals (along with 95% confidence upper limits) for the parameters defining the ensemble properties of the MSPs population; specifically, the in-band number of MSPs, $N_{\rm obs}$ and averaged ellipticity, μ_ϵ.

A. Significance

To compute the p value, we use the statistical property of the observed SNR of the overall amplitude $\rho_{\hat{A}}$ that it is a normal distributed random variable with zero mean and standard deviation 1 [see Eqs. (12) and (14)] in the absence of a signal. The results are summarized in Table I. The observed SNR from the $\mathrm{O1}+\mathrm{O2}+\mathrm{O3}$ dataset is $\rho_{\hat{A}}=0.92$ with p value $=18\%$, if the exponential density profile for the radial coordinate is considered. On the other hand, using the template with the Gaussian distributed radial coordinate, the observed SNR from the $\mathrm{O1}+\mathrm{O2}+\mathrm{O3}$ network is $\rho_{\hat{A}}=1.0$ with p value $=16\%$. The observed SNR is consistent with the Gaussian noise. Hence, the results conclude that, we do not find significant evidence for the SGWB from the Galactic millisecond pulsars. We also note that the current observational data is not sensitive enough to distinguish between the spatial distribution models.

B. Constraining the source parameters

The ensemble properties of the MSP population are inferred using the Bayesian analysis. As, we discussed in the previous sections, the PDF for the observed overall amplitude $\hat{A}$ can be assumed to be a Gaussian distribution with mean $A=N_{\rm obs}\mu_\epsilon^2$ and standard deviation $\sigma_{\hat{A}}$. The two sets of prior are considered: uniform and log-uniform prior distributions for $N_{\rm obs}$ and μ_ϵ over the ranges $[10^4, 10^5]$ and $[10^{-10}, 10^{-5}]$, respectively. Second, a log-uniform distribution considering the same maximum and minimum range for both the parameters. Given the likelihood and priors, the joint and marginalized posterior densities are computed numerically. The joint and marginalized posterior densities along with the median and 90% credible interval for the parameters are shown in Fig. 2. In this figure, we show four combinations, i.e., uniform and log uniform prior for the parameters along with the observed $\hat{A}$ using the $\mathrm{O1}+\mathrm{O2}+\mathrm{O3}$ network for the exponential and Gaussian density profiles. The best 95% confidence upper limits on the source parameters are obtained using the log-uniform prior: they are $\mu_\epsilon \leq 1.4\times10^{-6}$ and $N_{\rm obs}\leq 8.8\times10^4$. The limit on the averaged ellipticity μ_ϵ is consistent with the predicted minimum ellipticity of $\geq 10^{-9}$ [33].

TABLE I. Here, we report the results of the targeted stochastic search analysis using the data from the first three observing runs of Advanced LIGO (H and L) and Advanced Virgo (V) detectors, hence the five individual datasets, i.e., O3-HL, O3-LV, O3-HV, O2-HL, and O1-HL and with the combined network, $\mathrm{O1}+\mathrm{O2}+\mathrm{O3}$. The observed overall amplitude, $\hat{A}$ with the uncertainty, $\sigma_{\hat{A}}$ and SNR, $\rho_{\hat{A}}$ are obtained using the two templates for the spatial distribution created for the exponential and Gaussian distributed radial coordinate. The results are assessed through the p value against the null hypothesis, which is that the data is pure Gaussian noise. We do not claim any detection since the obtained p values do not pass the threshold, 5%.

$\mathrm{O1}+\mathrm{O2}+\mathrm{O3}$ results				
Baseline	Exponential radial distribution		Gaussian radial distribution	
	$(\hat{A}\pm\sigma_{\hat{A}})\times10^{-8}$	$\rho_{\hat{A}}$ (p value%)	$(\hat{A}\pm\sigma_{\hat{A}})\times10^{-8}$	$\rho_{\hat{A}}$ (p value%)
O3-HL	5.7 ± 6.2	0.92 (18)	3.4 ± 6.3	0.54 (30)
O3-HV	120 ± 53	2.3 (1.2)	96 ± 44	2.2 (1.4)
O3-LV	17 ± 31	0.54 (29)	59 ± 29	2.0 (2.1)
O2-HL	-17 ± 24	−0.69 (76)	-8.8 ± 25	−0.36 (64)
O1-HL	-54 ± 51	−1.1 (85)	-56 ± 53	−1.1 (86)
O1 + O2 + O3	$\mathbf{5.4\pm5.8}$	**0.92 (18)**	$\mathbf{5.9\pm5.9}$	**1.0 (16)**

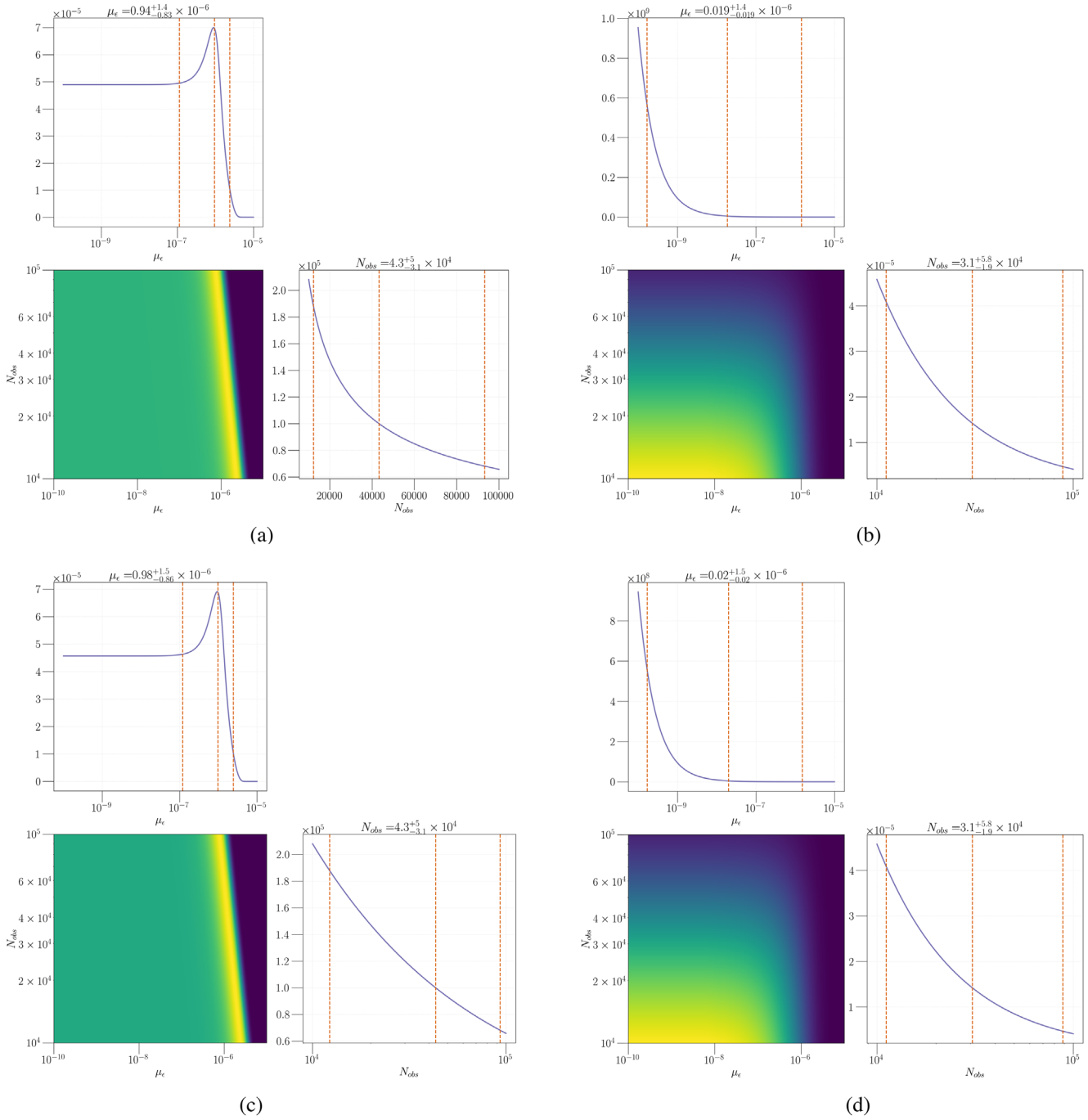

FIG. 2. The corner plot depicts the joint and marginalized posterior density for the source parameters ($N_{\rm obs}$ and μ_ϵ) using the O1 + O2 + O3 data. The prior for the parameters are uniform (left) or log-uniform (right) over parameter ranges $\mu_\epsilon \in [10^{-10}, 10^{-5}]$ and $N_{\rm obs} \in [10^4, 10^5]$. The dashed lines (and title) in the 1D plot show the median values along with the (0.05,0.95) quantile values. The caption for each subplot shows the combination of radial density profile and assumed priors. (a) Exponential distribution and uniform prior (b) Exponential distribution and log-uniform prior (c) Gaussian distribution and uniform prior and (d) Gaussian distribution and log-uniform prior.

VI. FUTURE SENSITIVITY OF THE SEARCH

Given the successful completion of the O3 run of Advanced LIGO and Advanced Virgo detectors, the upgrades of second-generation (2G) detectors are planned and aim to achieve the Advanced LIGO Plus (A+) and Advanced Virgo Plus (AdV+) sensitivity during the fifth observing run. Along with the KAGRA detector, situated in Japan (K, [67–69]), which has started its operation, they will be joined by the LIGO-India observatory (I, [70,71]), which is planned for construction in Hingoli, India with

A+ sensitivity. Other than that, the third-generation (3G) observatories such as Cosmic Explorer [72] and ET [73] are also envisioned for the future. The design sensitivities of these detectors are shown in top panel of Fig. 3 using the publicly available projected noise sensitivity curves [72,74,75]. As the detector network grows and the sensitivities of the detectors improve, it will be interesting to get an idea about the sensitivity of the stochastic targeted search to the parameters of the Galactic MSPs population. We measure the sensitivity of the average ellipticity μ_ϵ through the expected SNR of the overall amplitude $\langle \rho_{\hat{A}} \rangle$ using Eqs. (11), (12), and (14) given as

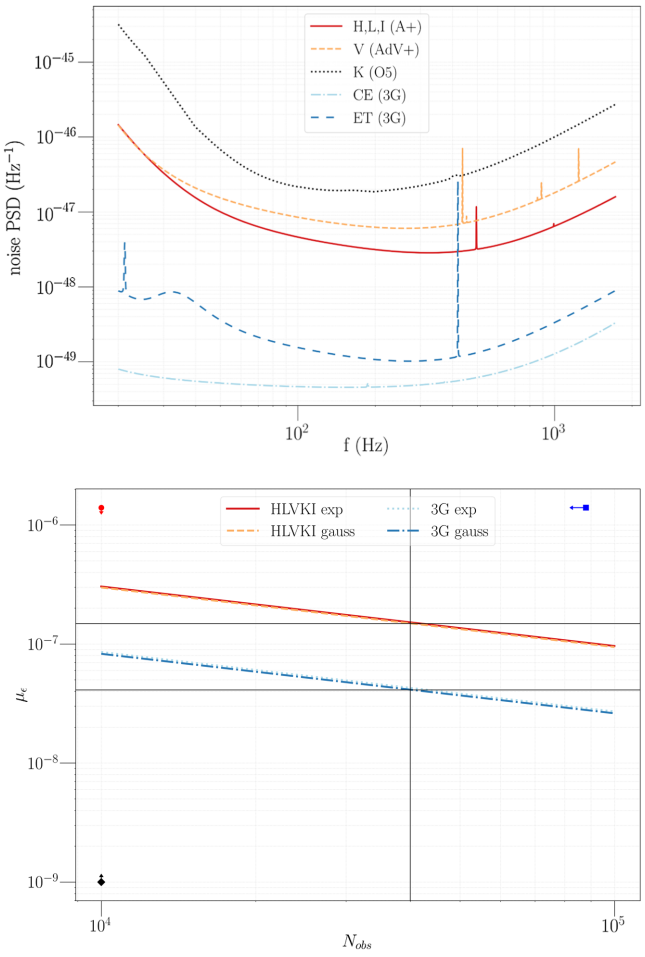

FIG. 3. The top panel represents the assumed noise curves for the considered 2G and 3G detectors. In the bottom panel, we show the one-sigma sensitivity of the future detector networks in the $N_{\rm obs}$-μ_ϵ plane for the exponential and Gaussian density profiles for one year of the observational run. [a] The horizontal solid lines show the achievable 1-sigma sensitivity for μ_ϵ if the in-band pulsars are $N_{\rm obs} = 40000$ in total with the 2G and 3G detectors. The arrows with the circle, the square, and the diamond at its end show the 95% confidence upper limits set on μ_ϵ and $N_{\rm obs}$ and the predicted lower limit on ellipticity in [33]. [a] Even though Einstein Telescope (ET) is planned to have three colocated detectors [73], we only considered one detector (ET1) for our test study.

$$\langle \rho_{\hat{A}} \rangle = A\sqrt{\hat{\mathcal{P}}^\dagger \mathbf{\Gamma} \hat{\mathcal{P}}} = N_{\rm obs}\mu_\epsilon^2 \left[T_{\rm days} \sum\nolimits_{\mathcal{I},t_i,f} \frac{\hat{\mathcal{P}}^*_\alpha \gamma^{\mathcal{I}*}_\alpha(t_i;f)\gamma^{\mathcal{I}}_{\alpha'}(t_i;f)\hat{\mathcal{P}}_{\alpha'}\bar{H}_f^2}{P_1(f)P_2(f)} \right]^{1/2}. \tag{23}$$

Here, we assume that i runs from 0 to the number of segments in one sidereal day, the data is taken for $T_{\rm days}$ number of sidereal days, and the noise is stationary during the whole observing run. We note that the SNR is proportional to the square root of the number of total segments (or days) and the frequency bins. In the bottom panel of Fig. 3, we show the one-sigma sensitivity (i.e., $\langle \rho_{\hat{A}} \rangle = 1$) in $N_{\rm obs}$-μ_ϵ plane for both the exponential and Gaussian density profile considering one year of observations with multiple detector network. Here, we have considered a network of five 2G detectors (H, L, V, K, and I) with A+ sensitivity, and for the 3G case, one baseline was formed by assuming one Cosmic Explorer detector in the USA (assuming the location of the Hanford detector) and one ET in Europe (assuming the location of the Virgo detector).

We note here that, with the 2G detector network with A+ sensitivity, for the optimal number of in-band NSs, $N_{\rm obs} = 40000$ [28], one-sigma sensitivity for μ_ϵ is $\sim 1.5 \times 10^{-7}$. Considering the GW detector network with all 2G detectors simultaneously (the HLVKI network) gives only marginal improvement compared to the HL network since the latter favors ORF dominantly. With the 3G detector network, we might achieve $\sim 4.1 \times 10^{-8}$ sensitivity which is close to the minimum limit on the ellipticity [33].

VII. CONCLUSIONS

We performed a targeted stochastic search for the Galactic millisecond pulsars using the O1, O2, and O3 data from the Advanced LIGO's Hanford and Livingston and Advanced Virgo detector. In this search, we assumed that the shape of the spectra and spatial distribution of SGWB from the source population is known *a priori* from the theory and the electromagnetic observations. The analysis found that the data is consistent with the noise, favoring the null hypothesis. Hence, we constrained the ensemble properties of the source population, i.e., the in-band number of MSPs, $N_{\rm obs}$ and averaged ellipticity, μ_ϵ using the Bayesian formalism. We found that the log-uniform prior for the source properties gives the best 95% confidence upper limits, i.e., $\mu_\epsilon \leq 1.4 \times 10^{-6}$ and $N_{\rm obs} \leq 8.8 \times 10^4$. Even though the error bars on our results with the current data are relatively large, we expect them to narrow down with the future network of detectors. We show that with the 3G detectors, we might achieve $\sim 4.1 \times 10^{-8}$ sensitivity, which is close to the minimum limit on the ellipticity [33].

Meanwhile, many searches have been proposed and performed to set limits on the MSP properties. Recently,

matched filtering based targeted search [32] for the GWs from individual MSP (PSR J0711–6830) has set upper limits on the ellipticity $\epsilon \leq 5.3 \times 10^{-9}$. These searches model the phase evolution of the GW signal given the source parameters, e.g., period, period derivatives, and location in the sky. These searches are more sensitive if the parameter values are known from the electromagnetic observations and the sensitivity degrades considerably for sources with unknown parameters. By performing a hierarchical Bayesian formalism using the GW observation data for known individual pulsars, one can infer the hyperparameters describing the ellipticity distribution (e.g., mean and variance of the ellipticity, if it is Gaussian distributed). In a recent work Pitkin *et al.* [76] use this approach and provides the upper limit for the mean ellipticity using the data from LIGO's sixth science run. The search outlined in our paper complements the matched filtering-based targeted searches. Our method is faster and probes the sources with minimal assumptions for the parameters (i.e., if the only frequency and sky distribution are known). It will be interesting to jointly constrain the ensemble properties using observations from the targeted searches and stochastic searches [21]. On the other hand, our results are found to be consistent with the upper limits reported in [76]. Recently, De Lillo *et al.* [22] also inferred the average ellipticity of the Galactic and extragalactic population of the MSPs using the cross-correlation method for SGWBs (as a function of the number of the neutron stars emitting GWs within the frequency band of the search). Given the isotropic background assumptions (this may lead to conservative limits) and the difference in the pulsar population properties, the results are not straightforward to compare with our template-based search.

It is interesting to note that one can easily extend this work in several directions. One, the actual distribution of the source may differ from the specific spin period, and spatial distribution adapted in our analysis. Hence one can explore the changes in the sensitivity of the search to the variations in source distributions. Second, the uncertainty in the assumed values for the parameter $\langle I^2 \rangle$ may play an important role in our analysis. Accounting for this uncertainty can further benefit similar searches in the future. Third, the hyperparameters for the spectral shape, (μ, σ) in Eq. (18) and spatial distribution, $(R_0, z_0/\Sigma_r)$ in Eqs. (19) and (20) can be treated as free parameters. Then, one could use the all-sky all-frequency search results [77] to perform a parameter estimation [23]. Finally, since the perturbations in the cosmological scale can lead to the anisotropic stochastic background, many models [9–13] can be studied using the formalism discussed in this work.

ACKNOWLEDGMENTS

The authors thank Patrick Meyers for carefully reading the manuscript and providing valuable comments. This work significantly benefitted from the interactions with the Stochastic Working Group of the LIGO-Virgo-KAGRA Scientific Collaboration. This material is based upon work supported by NSF's LIGO Laboratory, which is a major facility fully funded by the National Science Foundation. The authors are grateful for computational resources provided by the LIGO Laboratory (CIT) supported by National Science Foundation Grants No. PHY-0757058 and No. PHY-0823459, and Inter-University Center for Astronomy and Astrophysics (Sarathi). This research has made use of data or software obtained from the Gravitational Wave Open Science Center [78], a service of LIGO Laboratory, the LIGO Scientific Collaboration, the Virgo Collaboration, and KAGRA. LIGO Laboratory and Advanced LIGO are funded by the United States National Science Foundation (NSF) as well as the Science and Technology Facilities Council (STFC) of the United Kingdom, the Max-Planck-Society (MPS), and the State of Niedersachsen/Germany for support of the construction of Advanced LIGO and construction and operation of the GEO600 detector. Additional support for Advanced LIGO was provided by the Australian Research Council. Virgo is funded, through the European Gravitational Observatory (EGO), by the French Centre National de Recherche Scientifique (CNRS), the Italian Istituto Nazionale di Fisica Nucleare (INFN) and the Dutch Nikhef, with contributions by institutions from Belgium, Germany, Greece, Hungary, Ireland, Japan, Monaco, Poland, Portugal, and Spain. The construction and operation of KAGRA are funded by Ministry of Education, Culture, Sports, Science and Technology (MEXT), and Japan Society for the Promotion of Science (JSPS), National Research Foundation (NRF) and Ministry of Science and ICT (MSIT) in Korea, Academia Sinica (AS) and the Ministry of Science and Technology (MoST) in Taiwan. This article has a LIGO document number LIGO-P2200056. We used numerous software packages such as NumPy [79], SciPy [80], ASTROPY [81], PyStoch [66], BILBY [82,83], DYNESTY [84], PyMultiNest [85], and MATPLOTLIB [86] in this work. We also used the locations information for the detectors (K, I, ET-A) available in the PyCBC package [87,88].

APPENDIX: DERIVATION OF THE PSD FOR THE MSP POPULATION

The SGWB can be characterized using a dimensionless energy density parameter which has a unit of $\mathrm{Hz}^{-1}\,\mathrm{sr}^{-1}$ defined as [24]

$$\Omega_{\mathrm{gw}}(f, \hat{\Omega}) = \frac{f}{\rho_c} \frac{\mathrm{d}\rho_{\mathrm{gw}}}{\mathrm{d}f \mathrm{d}^2\hat{\Omega}}, \tag{A1}$$

where ρ_{gw} is the energy density of the GWs emitted in frequency range f and $f + \mathrm{d}f$ per unit solid angle and $\rho_c = 3H_0^2c^2/8\pi G$ is the critical energy density for a flat universe. If, we assume that the SGWB is the resultant of the incoherent sum of GW power from $N(f, \hat{\Omega})$ number of sources in the frequency range f to $f + \mathrm{d}f$ and lying in solid angle $\hat{\Omega}$ and $\hat{\Omega} + \mathrm{d}^2\hat{\Omega}$, then

$$\Omega_{\rm gw}(f,\hat{\Omega}) = \frac{f}{c\rho_c}\sum_{i=1}^{N(f,\hat{\Omega})}\frac{P^{(i)}}{4\pi r_{(i)}^2}\delta(f-f^{(i)})\delta^2(\hat{\Omega}-\hat{\Omega}^{(i)}). \quad \text{(A2)}$$

Here $P^{(i)}$ is the GW power radiated from a source at distance $r^{(i)}$ from Earth. Now, the luminosity of the radiated GWs from a deformed axis-symmetric spinning neutron star having moment of inertia I and ellipticity ϵ, emitting nearly monochromatic signal at frequency f is given by [89]

$$P = \frac{32\pi^6 G}{5c^5}\epsilon^2 I^2 f^6. \quad \text{(A3)}$$

Considering Eqs. (A2) and (A3), one can write

$$\Omega_{\rm gw}(f,\hat{\Omega}) = \frac{32\pi^6 G f}{5c^6\rho_c}\sum_{i=1}^{N(f,\hat{\Omega})}\frac{\epsilon_{(i)}^2 I_{(i)}^2 f_{(i)}^6}{4\pi r_{(i)}^2} \times \delta(f-f^{(i)})\delta^2(\hat{\Omega}-\hat{\Omega}^{(i)}), \quad \text{(A4)}$$

The above expression can be written in terms of population-averaged ($\langle..\rangle_s$) quantities as

$$\Omega_{\rm gw}(f,\hat{\Omega}) = \frac{8\pi^5 G}{5c^6\rho_c}N_{\rm obs}\langle\epsilon^2\rangle_s f^7 p(f)\langle I^2\rangle_s\langle r^{-2}\rangle_s p(\hat{\Omega}). \quad \text{(A5)}$$

Additionally, the dimensionless energy density parameter is related to the source PSD as [24]

$$\Omega_{\rm gw}(f,\hat{\Omega}) = \frac{2\pi^2}{3H_0^2}f^3\mathcal{P}(f,\hat{\Omega}). \quad \text{(A6)}$$

Therefore the source PSD can be written as

$$\mathcal{P}(f,\hat{\Omega}) = \frac{32\pi^4 G^2}{5c^8}N_{\rm obs}\langle\epsilon^2\rangle_s f^4 p(f)\langle I^2\rangle_s\langle r^{-2}\rangle_s p(\hat{\Omega}). \quad \text{(A7)}$$

[1] LIGO Scientific and Virgo Collaborations *et al.*, Gwtc-2.1: Deep extended catalog of compact binary coalescences observed by LIGO and Virgo during the first half of the third observing run, arXiv:2108.01045.

[2] LIGO Scientific, Virgo, and KAGRA Collaborations *et al.*, Gwtc-3: Compact binary coalescences observed by LIGO and Virgo during the second part of the third observing run, arXiv:2111.03606.

[3] Alexander H. Nitz, Sumit Kumar, Yi-Fan Wang, Shilpa Kastha, Shichao Wu, Marlin Schäfer, Rahul Dhurkunde, and Collin D. Capano, 4-ogc: Catalog of gravitational waves from compact-binary mergers, arXiv:2112.06878.

[4] J. Aasi, B. P. Abbott *et al.*, Advanced LIGO, Classical Quantum Gravity **32**, 074001 (2015).

[5] F. Acernese, M. Agathos *et al.*, Advanced Virgo: A second-generation interferometric gravitational wave detector, Classical Quantum Gravity **32**, 024001 (2015).

[6] Rodrigo Tenorio, David Keitel, and Alicia M. Sintes, Search methods for continuous gravitational-wave signals from unknown sources in the advanced-detector era, Universe **7**, 474 (2021).

[7] Joseph D. Romano and Neil. J. Cornish, Detection methods for stochastic gravitational-wave backgrounds: A unified treatment, Living Rev. Relativity **20**, 2 (2017).

[8] N. Mazumder, S. Mitra, and S. Dhurandhar, Astrophysical motivation for directed searches for a stochastic gravitational wave background, Phys. Rev. D **89**, 084076 (2014).

[9] Alexander C. Jenkins and Mairi Sakellariadou, Anisotropies in the stochastic gravitational-wave background: Formalism and the cosmic string case, Phys. Rev. D **98**, 063509 (2018).

[10] A. C. Jenkins, M. Sakellariadou, T. Regimbau, and E. Slezak, Anisotropies in the astrophysical gravitational-wave background: Predictions for the detection of compact binaries by LIGO and Virgo, Phys. Rev. D **98**, 063501 (2018).

[11] Pablo A. Rosado, Gravitational wave background from rotating neutron stars, Phys. Rev. D **86**, 104007 (2012).

[12] Cheng-Jian Wu, Vuk Mandic, and Tania Regimbau, Accessibility of the stochastic gravitational wave background from magnetars to the interferometric gravitational wave detectors, Phys. Rev. D **87**, 042002 (2013).

[13] Paul D. Lasky, Mark F. Bennett, and Andrew Melatos, Stochastic gravitational wave background from hydrodynamic turbulence in differentially rotating neutron stars, Phys. Rev. D **87**, 063004 (2013).

[14] Giulia Cusin, Cyril Pitrou, and Jean-Philippe Uzan, Anisotropy of the astrophysical gravitational wave background: Analytic expression of the angular power spectrum and correlation with cosmological observations, Phys. Rev. D **96**, 103019 (2017).

[15] Giulia Cusin, Irina Dvorkin, Cyril Pitrou, and Jean-Philippe Uzan, First Predictions of the Angular Power Spectrum of the Astrophysical Gravitational Wave Background, Phys. Rev. Lett. **120**, 231101 (2018).

[16] Giulia Capurri, Andrea Lapi, Carlo Baccigalupi, Lumen Boco, Giulio Scelfo, and Tommaso Ronconi, Intensity and anisotropies of the stochastic gravitational wave background from merging compact binaries in galaxies, J. Cosmol. Astropart. Phys. 11 (2021) 032.

[17] Daniele Bertacca, Angelo Ricciardone, Nicola Bellomo, Alexander C. Jenkins, Sabino Matarrese, Alvise Raccanelli, Tania Regimbau, and Mairi Sakellariadou, Projection effects

on the observed angular spectrum of the astrophysical stochastic gravitational wave background, Phys. Rev. D **101**, 103513 (2020).
[18] Nicola Bellomo, Daniele Bertacca, Alexander C. Jenkins, Sabino Matarrese, Alvise Raccanelli, Tania Regimbau, Angelo Ricciardone, and Mairi Sakellariadou, CLASS_GWB: Robust modeling of the astrophysical gravitational wave background anisotropies, J. Cosmol. Astropart. Phys. 06 (2022) 030.
[19] Cyril Pitrou, Giulia Cusin, and Jean-Philippe Uzan, Unified view of anisotropies in the astrophysical gravitational-wave background, Phys. Rev. D **101**, 081301 (2020).
[20] Tania Regimbau, The quest for the astrophysical gravitational-wave background with terrestrial detectors, Symmetry **14**, 270 (2022).
[21] Dipongkar Talukder, Eric Thrane, Sukanta Bose, and Tania Regimbau, Measuring neutron-star ellipticity with measurements of the stochastic gravitational-wave background, Phys. Rev. D **89**, 123008 (2014).
[22] Federico De Lillo, Jishnu Suresh, and Andrew L. Miller, Stochastic gravitational-wave background searches and constraints on neutron-star ellipticity, Mon. Not. R. Astron. Soc. **513**, 1105 (2022).
[23] R. Abbott, T. D. Abbott *et al.* (LIGO Scientific, Virgo, and KAGRA Collaborations), Upper limits on the isotropic gravitational-wave background from Advanced LIGO and Advanced Virgo's third observing run, Phys. Rev. D **104**, 022004 (2021).
[24] R. Abbott, T. D. Abbott *et al.* (LIGO Scientific, Virgo, and KAGRA Collaborations), Search for anisotropic gravitational-wave backgrounds using data from Advanced LIGO and Advanced Virgo's first three observing runs, Phys. Rev. D **104**, 022005 (2021).
[25] Eric Thrane, Stefan Ballmer, Joseph D. Romano, Sanjit Mitra, Dipongkar Talukder, Sukanta Bose, and Vuk Mandic, Probinalactic the anisotropies of a stochastic gravitational-wave background using a network of ground-based laser interferometers, Phys. Rev. D **80**, 122002 (2009).
[26] Dipongkar Talukder, Sanjit Mitra, and Sukanta Bose, Multibaseline gravitational wave radiometry, Phys. Rev. D **83**, 063002 (2011).
[27] N. Sartore, E. Ripamonti, A. Treves, and R. Turolla, Galactic neutron stars—I. Space and velocity distributions in the disk and in the halo, Astron. Astrophys. **510**, A23 (2010).
[28] Duncan R. Lorimer, The galactic millisecond pulsar population, Proc. Int. Astron. Union **8**, 237 (2012).
[29] Paul D. Lasky, Gravitational waves from neutron stars: A review, Pub. Astron. Soc. Aust. **32**, e034 (2015).
[30] Fabian Gittins and Nils Andersson, Modelling neutron star mountains in relativity, Mon. Not. R. Astron. Soc. **507**, 116 (2021).
[31] Curt Cutler, Gravitational waves from neutron stars with large toroidal *b* fields, Phys. Rev. D **66**, 084025 (2002).
[32] LIGO Scientific, Virgo, and KAGRA Collaborations *et al.*, Searches for gravitational waves from known pulsars at two harmonics in the second and third LIGO-Virgo observing runs, arXiv:2111.13106.
[33] G. Woan, M. D. Pitkin, B. Haskell, D. I. Jones, and P. D. Lasky, Evidence for a minimum ellipticity in millisecond pulsars, Astrophys. J. **863**, L40 (2018).
[34] Sanjeev Dhurandhar, Hideyuki Tagoshi, Yuta Okada, Nobuyuki Kanda, and Hirotaka Takahashi, Cross-correlation search for a hot spot of gravitational waves, Phys. Rev. D **84**, 083007 (2011).
[35] Francesca Calore, Tania Regimbau, and Pasquale Dario Serpico, Probing the Fermi-LAT GeV Excess with Gravitational Waves, Phys. Rev. Lett. **122**, 081103 (2019).
[36] Stefan W. Ballmer, A radiometer for stochastic gravitational waves, Classical Quantum Gravity **23**, S179 (2006).
[37] Sanjit Mitra, Sanjeev Dhurandhar, Tarun Souradeep, Albert Lazzarini, Vuk Mandic, Sukanta Bose, and Stefan Ballmer, Gravitational wave radiometry: Mapping a stochastic gravitational wave background, Phys. Rev. D **77**, 042002 (2008).
[38] Anirban Ain, Prathamesh Dalvi, and Sanjit Mitra, Fast gravitational wave radiometry using data folding, Phys. Rev. D **92**, 022003 (2015).
[39] Bruce Allen, Warren G. Anderson, Patrick R. Brady, Duncan A. Brown, and Jolien D. E. Creighton, Findchirp: An algorithm for detection of gravitational waves from inspiraling compact binaries, Phys. Rev. D **85**, 122006 (2012).
[40] Sambit Panda, Swetha Bhagwat, Jishnu Suresh, and Sanjit Mitra, Stochastic gravitational wave background mapmaking using regularized deconvolution, Phys. Rev. D **100**, 043541 (2019).
[41] Deepali Agarwal, Jishnu Suresh, Sanjit Mitra, and Anirban Ain, Upper limits on persistent gravitational waves using folded data and the full covariance matrix from Advanced LIGO's first two observing runs, Phys. Rev. D **104**, 123018 (2021).
[42] Arianna I. Renzini and Carlo R. Contaldi, Gravitational-Wave Background Sky Maps from Advanced LIGO O1 Data, Phys. Rev. Lett. **122**, 081102 (2019).
[43] A. I. Renzini and C. R. Contaldi, Improved limits on a stochastic gravitational-wave background and its anisotropies from Advanced LIGO O1 and O2 runs, Phys. Rev. D **100**, 063527 (2019).
[44] Aaron Worley, Plamen G. Krastev, and Bao-An Li, Nuclear constraints on the momenta of inertia of neutron stars, Astrophys. J. **685**, 390 (2008).
[45] Sarah A. Story, Peter L. Gonthier, and Alice K. Harding, Population synthesis of radio and γ-ray millisecond pulsars from the galactic disk, Astrophys. J. **671**, 713 (2007).
[46] D. R. Lorimer, P. Esposito, R. N. Manchester, A. Possenti, A. G. Lyne, M. A. McLaughlin, M. Kramer, G. Hobbs, I. H. Stairs, M. Burgay, R. P. Eatough, M. J. Keith, A. J. Faulkner, N. D'Amico, F. Camilo, A. Corongiu, and F. Crawford, The Parkes multibeam pulsar survey—VII. Timing of four millisecond pulsars and the underlying spin-period distribution of the Galactic millisecond pulsar population, Mon. Not. R. Astron. Soc. **450**, 2185 (2015).
[47] T. Grégoire and J. Knödlseder, Constraining the galactic millisecond pulsar population using Fermi Large Area Telescope, Astron. Astrophys. **554**, A62 (2013).
[48] D. R. Lorimer, F. Camilo, and M. A. McLaughlin, Timing of pulsars found in a deep Parkes multibeam survey, Mon. Not. R. Astron. Soc. **434**, 347 (2013).
[49] M. Burgay, M. J. Keith, D. R. Lorimer, T. E. Hassall, A. G. Lyne, F. Camilo, N. D'Amico, G. B. Hobbs, M. Kramer, R. N. Manchester, M. A. McLaughlin, A. Possenti,

I. H. Stairs, and B. W. Stappers, The Perseus Arm Pulsar Survey, Mon. Not. R. Astron. Soc. **429**, 579 (2013).
[50] M. Burgay, B. C. Joshi, N. D'Amico, A. Possenti, A. G. Lyne, R. N. Manchester, M. A. McLaughlin, M. Kramer, F. Camilo, and P. C. C. Freire, The Parkes High-Latitude pulsar survey, Mon. Not. R. Astron. Soc. **368**, 283 (2006).
[51] B. A. Jacoby, M. Bailes, S. M. Ord, R. T. Edwards, and S. R. Kulkarni, A large-area survey for radio pulsars at high galactic latitudes, Astrophys. J. **699**, 2009 (2009).
[52] R. T. Edwards, M. Bailes, W. van Straten, and M. C. Britton, The Swinburne intermediate-latitude pulsar survey, Mon. Not. R. Astron. Soc. **326**, 358 (2001).
[53] R. N. Manchester, A. G. Lyne, F. Camilo, J. F. Bell, V. M. Kaspi, N. D'Amico, N. P. F. McKay, F. Crawford, I. H. Stairs, A. Possenti, M. Kramer, and D. C. Sheppard, The Parkes multi-beam pulsar survey—I. Observing and data analysis systems, discovery and timing of 100 pulsars, Mon. Not. R. Astron. Soc. **328**, 17 (2001).
[54] R. Abuter *et al.* (Gravity Collaboration), Detection of the gravitational redshift in the orbit of the star s2 near the galactic centre massive black hole, Astron. Astrophys. **615**, L15 (2018).
[55] Morgan Bennett and Jo Bovy, Vertical waves in the solar neighbourhood in Gaia DR2, Mon. Not. R. Astron. Soc. **482**, 1417 (2019).
[56] K. M. Gorski, Eric Hivon, A. J. Banday, B. D. Wandelt, F. K. Hansen, M. Reinecke, and M. Bartelman, HEALPix—A framework for high resolution discretization, and fast analysis of data distributed on the sphere, Astrophys. J. **622**, 759 (2005).
[57] Andrea Zonca, Leo P. Singer, Daniel Lenz, Martin Reinecke, Cyrille Rosset, Eric Hivon, and Krzysztof M. Gorski, healpy: Equal area pixelization and spherical harmonics transforms for data on the sphere in Python, J. Open Source Softwaare **4**, 1298 (2019).
[58] Ling Sun *et al.*, Characterization of systematic error in advanced LIGO calibration, Classical Quantum Gravity **37**, 225008 (2020).
[59] F. Acernese *et al.*, Calibration of Advanced Virgo and reconstruction of the detector strain h(t) during the observing run O3, Classical Quantum Gravity **39**, 045006 (2022).
[60] D. Davis *et al.*, LIGO detector characterization in the second and third observing runs, Classical Quantum Gravity **38**, 135014 (2021).
[61] Rich Abbott, Thomas D. Abbott *et al.*, Open data from the first and second observing runs of Advanced LIGO and Advanced Virgo, SoftwareX **13**, 100658 (2021).
[62] https://www.gw-openscience.org/O3/.
[63] Benjamin P. Abbott *et al.* (LIGO Scientific and Virgo Collaborations), Directional Limits on Persistent Gravitational Waves from Advanced LIGO's First Observing Run, Phys. Rev. Lett. **118**, 121102 (2017).
[64] B. P. Abbott, R. Abbott *et al.* (LIGO Scientific and Virgo Collaborations), Directional limits on persistent gravitational waves using data from Advanced LIGO's first two observing runs, Phys. Rev. D **100**, 062001 (2019).
[65] LIGO Scientific, Virgo, and KAGRA Collaborations, *Folded data for first three observing runs of Advanced LIGO and Advanced Virgo* (Zenodo, 2022), 10.5281/zenodo.6326656.
[66] Anirban Ain, Jishnu Suresh, and Sanjit Mitra, Very fast stochastic gravitational wave background map making using folded data, Phys. Rev. D **98**, 024001 (2018).
[67] Kentaro Somiya, Detector configuration of KAGRA—The Japanese cryogenic gravitational-wave detector, Classical Quantum Gravity **29**, 124007 (2012).
[68] Yoichi Aso, Yuta Michimura, Kentaro Somiya, Masaki Ando, Osamu Miyakawa, Takanori Sekiguchi, Daisuke Tatsumi, and Hiroaki Yamamoto (KAGRA Collaboration), Interferometer design of the KAGRA gravitational wave detector, Phys. Rev. D **88**, 043007 (2013).
[69] T. Akutsu *et al.*, Overview of KAGRA: Detector design and construction history (2020).
[70] B. Iyer, T. Souradeep, C. S. Unnikrishnan, S. Dhurandhar, S. Raja, A. Kumar, and A. Sengupta, Proposal of the Consortium for Indian Initiative in Gravitational-wave Observations (IndIGO), LIGO-India Technical Report No. LIGO-M1100296, 2011.
[71] M. Saleem, Javed Rana, V. Gayathri, Aditya Vijaykumar, Srashti Goyal, Surabhi Sachdev, Jishnu Suresh, S. Sudhagar, Arunava Mukherjee, Gurudatt Gaur, Bangalore Sathyaprakash, Archana Pai, Rana X. Adhikari, P. Ajith, and Sukanta Bose, The science case for LIGO-India, Classical Quantum Gravity **39**, 025004 (2022).
[72] B. P. Abbott, R. Abbott *et al.*, Exploring the sensitivity of next generation gravitational wave detectors, Classical Quantum Gravity **34**, 044001 (2017).
[73] M. Punturo, M. Abernathy *et al.*, The Einstein telescope: A third-generation gravitational wave observatory, Classical Quantum Gravity **27**, 194002 (2010).
[74] LIGO, Virgo, and KAGRA Collaborations, Noise curves used for simulations in the update of the observing scenarios paper, Technical Report No. LIGO-T2000012-v1, 2022.
[75] Kevin Kuns, Evan Hall *et al.*, Cosmic explorer strain sensitivity, Technical Report No. CE-T2000017-v4, 2021.
[76] M. Pitkin, C. Messenger, and X. Fan, Hierarchical Bayesian method for detecting continuous gravitational waves from an ensemble of pulsars, Phys. Rev. D **98**, 063001 (2018).
[77] R. Abbott *et al.*, All-sky, all-frequency directional search for persistent gravitational-waves from Advanced LIGO's and Advanced Virgo's first three observing runs, Phys. Rev. D **105**, 122001 (2022).
[78] https://www.gw-openscience.org/.
[79] Stefan van der Walt, S. Chris Colbert, and Gael Varoquaux, The NumPy array: A structure for efficient numerical computation, Comput. Sci. Eng. **13**, 22 (2011).
[80] Pauli Virtanen *et al.*, SciPy 1.0: Fundamental algorithms for scientific computing in Python, Nat. Methods **17**, 261 (2020).
[81] A. M. Price-Whelan *et al.*, The Astropy Project: Building an open-science project and status of the v2.0 core package, Astron. J. **156**, 123 (2018).
[82] Gregory Ashton *et al.*, Bilby: A user-friendly Bayesian inference library for gravitational-wave astronomy, Astrophys. J. Suppl. Ser. **241**, 27 (2019).
[83] I. M. Romero-Shaw *et al.*, Bayesian inference for compact binary coalescences with Bilby: Validation and application to the first LIGO-Virgo gravitational-wave transient catalogue, Mon. Not. R. Astron. Soc. **499**, 3295 (2020).

[84] Joshua S. Speagle, dynesty: A dynamic nested sampling package for estimating Bayesian posteriors and evidences, Mon. Not. R. Astron. Soc. **493**, 3132 (2020).

[85] J. Buchner, A. Georgakakis, K. Nandra, L. Hsu, C. Rangel, M. Brightman, A. Merloni, M. Salvato, J. Donley, and D. Kocevski, X-ray spectral modelling of the AGN obscuring region in the CDFS: Bayesian model selection and catalogue, Astron. Astrophys. **564**, A125 (2014).

[86] J. D. Hunter, Matplotlib: A 2d graphics environment, Comput. Sci. Eng. **9**, 90 (2007).

[87] Tito Dal Canton, Alexander H. Nitz, Andrew P. Lundgren, Alex B. Nielsen, Duncan A. Brown, Thomas Dent, Ian W. Harry, Badri Krishnan, Andrew J. Miller, Karl Wette, Karsten Wiesner, and Joshua L. Willis, Implementing a search for aligned-spin neutron star-black hole systems with advanced ground based gravitational wave detectors, Phys. Rev. D **90**, 082004 (2014).

[88] Samantha A. Usman *et al.*, The PyCBC search for gravitational waves from compact binary coalescence, Classical Quantum Gravity **33**, 215004 (2016).

[89] Michele Maggiore, *Gravitational Waves. Vol. 1: Theory and Experiments*, Oxford Master Series in Physics (Oxford University Press, New York, 2007).